Computer Methods in Applied Mechanics and Engineering 457 (2026) 119009

Contents lists available at ScienceDirect

Comput. Methods Appl. Mech. Engrg.

journal homepage: www.elsevier.com/locate/cma

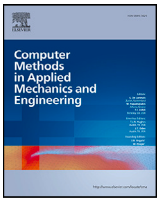

Efficient fluid structure interaction simulation of vocal fold oscillations using a homogenized Lattice Boltzmann Method

Adrian Kummerländer [a,b],*,[1], Bogac Tur [c],[1], Maik Haase [c], Fedor Bukreev [a,d], Michael Döllinger [c], Mathias J. Krause [a,b,d], Stefan Kniesburges [c],**

[a] *Lattice Boltzmann Research Group, Karlsruhe Institute of Technology, Karlsruhe, Germany*
[b] *Institute for Applied and Numerical Mathematics, Karlsruhe Institute of Technology, Englerstraße 2, Karlsruhe, 76131, Germany*
[c] *Division of Phoniatrics and Pediatric Audiology at the Department of Otorhinolaryngology, Head & Neck Surgery, Friedrich Alexander University Erlangen-Nürnberg, Waldstraße 1, Erlangen, 91054, Germany*
[d] *Institute for Mechanical Process Engineering and Mechanics, Karlsruhe Institute of Technology, Straße am Forum 8, Karlsruhe, 76131, Germany*

ARTICLE INFO

Keywords:
VF
CFD
FSI
LBM
HPC

ABSTRACT

Computational modeling of human phonation is a uniquely challenging fluid–structure interaction (FSI) problem. It is constrained both by the large computational cost and numerical restrictions of existing methods, particularly in handling vocal fold (VF) contact. To combine physiological fidelity with high computational efficiency, this study introduces a novel FSI coupling strategy in a highly optimized computational workflow. The core methodological advance lies in mapping the structural dynamics of a Six-Mass-Model (6MM) into a time-dependent porosity field, efficiently integrating it with a homogenized Lattice Boltzmann Method (HLBM) for the fluid dynamics. The fluid is modeled using the filtered Brinkman–Navier–Stokes equations, platform-transparently discretized by an HLBM variant in the OpenLB framework. By representing the moving VFs as a time-dependent porosity field, the solver implicitly handles complex geometry changes and contact without remeshing, while the two-way coupled 6MM captures both elastic motion and collision. Simulations in a 3D laryngeal channel produced stable, self-sustained oscillations at physiologically plausible values: fundamental frequency (f_0) ≈ 248 Hz, mean subglottal pressure ≈ 1.01 kPa, and an open quotient ≈ 0.64. The model robustly achieved complete glottal closure in each cycle, yielding credible peak contact forces (≈ 27 mN). Providing both high computational efficiency (up to 60 oscillation cycles/hour on a NVIDIA RTX 2000 Ada laptop GPU) and physiological results, the proposed HLBM-6MM solver enables systematic parameter studies of phonation previously infeasible with traditional FSI approaches.

1. Introduction

The human phonation process is the most important part of oral human communication [1]. It includes the flow-induced oscillation of the vocal folds (VFs) due to the exhalation flow [2,3]. Fig. 1 illustrates the anatomy of the human vocal tract and provides a simplified depiction of the myoelastic-aerodynamic phonation process, showing one vocal fold oscillation cycle.

---

* Corresponding author at: Institute for Applied and Numerical Mathematics, Karlsruhe Institute of Technology, Englerstraße 2, Karlsruhe, 76131, Germany.
** Corresponding author.
E-mail addresses: kummerlaender@kit.edu (A. Kummerländer), stefan.kniesburges@uk-erlangen.de (S. Kniesburges).

[1] These authors contributed equally to this work. Sorted alphabetically by last name.

https://doi.org/10.1016/j.cma.2026.119009
Received 5 December 2025; Received in revised form 4 March 2026; Accepted 14 April 2026

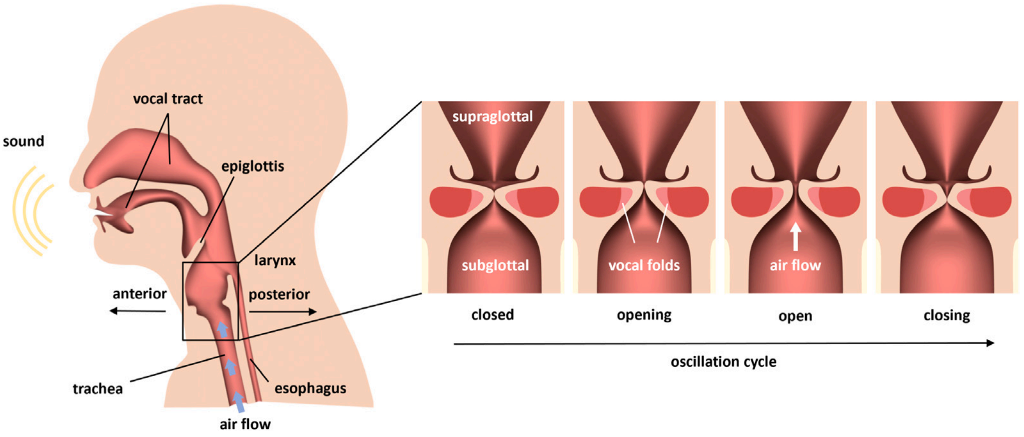

Fig. 1. Schematic illustration of the human phonatory mechanism during voice production. (Left) Sagittal view of the upper airway showing key structures relevant to phonation, including the epiglottis, larynx, vocal tract, and esophagus. (Right) Sequential views of the VFs showing the myoelastic-aerodynamic principle of vocal fold vibration for one oscillation cycle in the phases of closed, opening, open and closing.

As preparation for phonation, the VFs move towards each other in the larynx closing the airway passage into the lungs. During exhalation, the air is then pressed through the closed glottis, which is the gap between the pretensioned VFs. This induces self-sustained, three-dimensional oscillations of the VFs, characterized by the periodic opening and closing of the glottis, which modulates the expiratory airflow [4,5].

The flow above the oscillating VFs is characterized by a pulsatile jet flow which produces the basic acoustic signal of the vowels in human voice generation [3]. This basic acoustic signal is further transformed in the vocal tract (pharynx, oral and nasal cavities) adding additional frequencies, called formants, produced by resonance effects. Especially the first two formants are essential for the acoustic encoding of the vowels as their frequencies have characteristic frequencies for the different vowels [1,6,7].

From a physical modeling perspective, this process is described as a *fluid–structure-acoustic interaction* (FSAI) between the exhalation airflow, the myoelastic tissue of the VFs and the acoustic characteristics of the vocal tract [3,8]. Thereby, the coupling of the fluid flow and tissue dynamics is very strong and is characterized by immediate cross-interaction. In contrast, the coupling to the sound field is weaker, following a source-filter process for normal speech [9]. However, acoustic back-coupling effects on the voice source may occur described by non-linear source-filter theory [10,11]. It was found that tuning of fundamental frequency by the first vocal tract resonance occurring for frequencies up to 1300 Hz [12,13]. Meanwhile, the influence of vocal tract resonances in register changes or whistling register (>1500 Hz) is still part of current research [12].

In-vivo investigation of this highly complex FSAI process is very difficult as awake persons do not tolerate any sensors in the larynx. Even visualizing the VF oscillations is challenging, as the procedure of oral endoscopy itself is often poorly tolerated and can induce coughing or choking. Furthermore, while methods based on laser [4,14] or MRI [15] are being developed to capture the actual 3D VF dynamics and deformation, these approaches remain highly restricted. Laser-based endoscopic techniques, for instance, are limited to visualizing only the superior surfaces of the VFs. MRI-based methods are constrained by low temporal sampling frequencies (a few Hz), which is insufficient to adequately sample male VFs fully time-resolved even at a low fundamental frequency of 100 Hz.

As a consequence, many groups develop computational models that involve FSI or even FSAI processes [16–21]. Such models would, in principle, allow the analysis of the entire airway, from the mouth to the trachea. This involves the airway aerodynamics, the tissue deformation and stress fields and the acoustic production and modulation of the voice signal. However, computational modeling of voice production presents several significant challenges:

- Developing a valid material model of the multilayered composite VF tissue.
- Modeling of the contact mechanics between the VFs.
- Reducing the high numerical costs (both in walltime and hardware) for the computational fluid and structural dynamics.

Especially the collision and contact problem of the two VFs is still not sufficiently solved [21].

Previous FSI studies mainly applied the *Arbitrary Lagrangian Eulerian* (ALE) method for moving boundaries. In this case, the fluid flow and the tissue dynamics are discretized by two separate meshes and the momentum exchange occurs via the interfaces in between, i.e., the surfaces of the VFs [22–24]. The consequence of this approach is, that the cells of the fluid mesh collapse on contact between the VFs, a problem that cannot be handled by classic solvers for the *Navier–Stokes equations* (NSE) based on the *Finite Volume* (FVM) [25] or *Finite Element* (FEM) method. A common approach to evade this problem is to enforce a minimal glottal gap that maintains the integrity of the fluid mesh [21].

Another approach to handle the contact problem is the *Immersed Boundary Method* (IBM) [26–28]. IBM represents the interaction between fluid and solid geometries by locally adjusting the external force field of the NSE, i.e. the fluid mesh covers both the fluid and solid domain. This is based on tracing the interface between solid and fluid domain as a time-dependent function for the moving boundaries of the VFs. Although this enables contact between the two VFs, the computation of the interface still remains very complex and time consuming. This complexity is increased further by adaptive grid refinement for the fluid flow in regions with large pressure gradients. Nevertheless, there are various studies applying the IBM that managed to deliver insight into the physiology of the human phonation process [16,29].

In summary, although the FSI of human phonation can be simulated for isolated cases, large systematic studies of different phonation conditions for females, males, and children remain infeasible due to immense computational costs [25]. Studies focusing on FSI simulation typically apply commercial, open-source or in-house FVM NSE solvers, which require days or weeks to simulate even a single phonation case on massive parallel *High Performance Computing* (HPC) clusters. This presents a large drawback for scientists investigating differences between phonation cases, such as varying voice registers in professional singing.

Given these significant restrictions of existing methodology, this study introduces a novel computational approach to FSI simulation during phonation. Rather than proposing a fundamentally new fluid or structural discretization, the primary advance lies in the coupling strategy: it connects a *homogenized Lattice Boltzmann Method* (HLBM) used as a Brinkman-penalization solver [30–32] for the fluid part to a *Six-Mass-Model* (6MM) [33] for the solid part by representing the moving VFs as a time-dependent porosity field. This specific interface modeling implicitly handles complex geometry changes and self-contact, bypassing the mesh-collapse limitations of traditional ALE approaches and the complex interface-tracking of IBM. The combined model captures both the elastic motion and collision of the VFs driven by the fluid flow. It was implemented within the open-source LBM framework OpenLB [34,35] and utilizes modern *General Purpose Graphical Processing Units* (GPGPUs). By significantly reducing time-to-solution compared to traditional methods, this approach shifts the focus from isolated case studies to systematic parameter sweeps.

At the top level, the present paper is structured into a method (Section 2 and evaluation part (Section 3). The first part details the LB method (Section 2.1), the structure model (Section 2.2), the simulation setup (Section 2.3), as well as the data analysis approach (Section 2.4). The second part considers first the impact of the coupling time step (Section 3.1) followed by general characteristics (Section 3.2, glottal parameters (Section 3.3), supraglottal jet signatures (Section 3.4) and finally a parameter study of the mass model (Section 3.5).

2. Methods

2.1. Lattice Boltzmann method

Modeling the dynamics of VFs during phonation is particularly challenging for *computational fluid dynamics* (CFD) due to the interaction of transitional turbulent flow (∼1500 to 3000 Re) and the strongly deforming VF geometry which undergoes significant self-contacts during every oscillation cycle. In the present study we model this complex problem using the *filtered Brinkman–Navier–Stokes equations* (FBNSE), capturing both *large Eddy simulation* (LES) for subgrid-scale turbulence modeling and homogenized porous media for moving solid modeling in a single target equation. This equation was solved efficiently [36] in GPU-based simulations using a *homogenized lattice Boltzmann method* (HLBM) discretization [30,37] in OpenLB [34,35].

2.1.1. Filtered Brinkman–Navier–Stokes equations

The macroscopic motion of fluids is commonly described using the *Navier–Stokes equations* (NSE). Incompressible flows in heterogeneous domains consisting of both fully fluid regions and porous media can be described using the *filtered Brinkman–Navier–Stokes equations* (FBNSE)

$$\begin{cases} \boldsymbol{\nabla} \cdot \bar{\boldsymbol{u}} = 0, & \text{in } \Omega \times I, \\ \frac{\partial \bar{\boldsymbol{u}}}{\partial t} + \bar{\boldsymbol{u}} \cdot \boldsymbol{\nabla} \bar{\boldsymbol{u}} = -\frac{\boldsymbol{\nabla} \bar{p}}{\rho} + \nu_{\mathrm{mo}} \boldsymbol{\nabla}^2 \bar{\boldsymbol{u}} + \frac{\nu_{\mathrm{mo}}}{K} \bar{\boldsymbol{u}} - \boldsymbol{\nabla} \cdot \mathbf{T}_{\mathrm{sgs}}, & \text{in } \Omega \times I, \end{cases} \tag{1}$$

for filtered pressure $\bar{p}$, velocity $\bar{\boldsymbol{u}}$, density ρ on spatial domain $\Omega \subseteq \mathbb{R}^3$ and time $I \subseteq \mathbb{R}_{>0}$. The molecular kinematic viscosity is chosen as ν_{mo} and $K > 0$ the permeability coefficient of the porous medium. The term $\boldsymbol{\nabla} \cdot \mathbf{T}_{\mathrm{sgs}}$ models the subgrid-scale turbulence using the Smagorinsky LES approach

$$\nu_{\mathrm{turb}} = \left(C_{\mathrm{S}} \vartriangle x\right)^2 \left|\bar{\mathbf{S}}\right|, \tag{2}$$

$$\mathbf{T}_{\mathrm{sgs}} = 2\nu_{\mathrm{turb}} \bar{\mathbf{S}}, \tag{3}$$

where $C_{\mathrm{S}} > 0$ is the Smagorinsky constant, $\vartriangle x$ is the filter width, and $\bar{\mathbf{S}}$ is the filtered strain rate tensor

$$\bar{S}_{\alpha\beta} = \frac{1}{2} \left(\frac{\partial \bar{u}_\alpha}{\partial x_\beta} + \frac{\partial \bar{u}_\beta}{\partial x_\alpha} \right) \tag{4}$$

with $\alpha, \beta \in \{1, 2, 3\}$ being the spatial indices.

In the context of the present FSI approach, the FBNSE is not used to model a physical porous medium with an empirical permeability law such as the Forchheimer equation. Instead, the Brinkman drag term $\frac{\nu_{\mathrm{mo}}}{K} \bar{\boldsymbol{u}}$ is utilized as a volume penalization force. By treating the permeability coefficient K as a numerical tuning parameter, this term effectively enforces a no-slip boundary condition on the moving vocal folds. In the fully fluid domain $K \to \infty$ the penalty term vanishes, recovering the standard filtered NSE. Inside the solid domain, penalization is achieved by pushing K to its lowest numerically stable bound (cf. Eq. (12) in Section 2.1.2), forcing the local fluid velocity to match the solid boundary velocity.

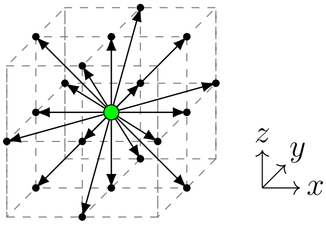

Fig. 2. Schematic of the discrete velocity set `D3Q19`. Green circle marks cell and arrows represent the discrete velocity vectors ξ_i as well as their target neighbor cells marked small black circles. Gray dashed lines overlay the uniform cartesian lattice. (For interpretation of the references to color in this figure legend, the reader is referred to the web version of this article.)

2.1.2. Homogenized lattice Boltzmann method

The HLBM is used to discretize the FBNSE (1) on a regular space–time grid with the `D3Q19` velocity stencil (cf. Fig. 2). Specifically, we utilize a *homogenized regularized recursive lattice Boltzmann method with Smagorinsky LES model* (HRRLBM-LES) that extends the classic HLBM [30] with a hybrid third-order recursive regularized collision model [38,39].

The filtered and homogenized LB equation is given by

$$f_i(\boldsymbol{x}+\xi_i \triangle t, t+\triangle t) = f_i^{\mathrm{eq}}(\boldsymbol{x},t) + \left(1-\frac{1}{\tau_{\mathrm{eff}}(\boldsymbol{x},t)}\right) f_i^{(1)}(\boldsymbol{x},t), \quad \text{in } \Omega_{\triangle x}\times I_{\triangle t}, \tag{5}$$

for distribution functions f_i along q discrete velocities ξ_i on a uniform cartesian lattice $\boldsymbol{x} \in \Omega_{\triangle x} \subset \Omega \subseteq \mathbb{R}^3$ with cell size $\triangle x$ at discrete times $t \in I_{\triangle t} \subset I \subseteq \mathbb{R}_{\geq 0}$ separated by step size $\triangle t$. The subgrid scale turbulence is accounted for by locally computing the effective relaxation time $\tau_{\mathrm{eff}}(\boldsymbol{x},t)$ using the Smagorinsky model

$$\tau_{\mathrm{eff}}(\boldsymbol{x},t) = \frac{\nu_{\mathrm{eff}}(\boldsymbol{x},t)}{c_{\mathrm{s}}^2}\frac{\triangle t}{\triangle x^2} + \frac{1}{2} \tag{6}$$

with *lattice speed of sound* c_s and local effective viscosity

$$\nu_{\mathrm{eff}}(\boldsymbol{x},t) = \nu_{\mathrm{mo}} + \nu_{\mathrm{turb}}(\boldsymbol{x},t) \tag{7}$$

utilizing the turbulent viscosity as given by Eq. (2).

The non-equilibrium distribution function $f_i^{(1)}$ is expanded in terms of Hermite polynomials $\mathbf{H}_i^{(n)}$ of the discrete velocity ξ_i as

$$f_i^{(1)}(\boldsymbol{x},t) = \omega_i \sum_{n=0}^{N=3} \frac{1}{c_{\mathrm{s}}^{2n} n!} \mathbf{H}_i^{(n)} : \mathbf{a}_1^{(n)}(\boldsymbol{x},t), \tag{8}$$

where ω_i are the lattice weights. The Hermite expansion coefficients are defined as

$$\mathbf{a}_1^{(n)}(\boldsymbol{x},t) = \sum_{i=0}^{q-1} \mathbf{H}_i^{(n)} f_i^{(1)}(\boldsymbol{x},t). \tag{9}$$

The equilibrium distribution function is defined as

$$f_i^{\mathrm{eq}}(\boldsymbol{x},t) = \omega_i \left(\rho + \frac{\xi_i \cdot \rho \hat{\mathbf{u}}}{c_{\mathrm{s}}^2} + \frac{\mathbf{H}_i^{(2)} : \hat{\mathbf{a}}_0^{(2)}}{2c_{\mathrm{s}}^4} + \frac{\mathbf{H}_i^{(3)} : \hat{\mathbf{a}}_0^{(3)}}{6c_{\mathrm{s}}^6} \right) \tag{10}$$

using Hermite coefficients $\hat{\mathbf{a}}_0^{(0)} = \rho(\boldsymbol{x},t)$ and $\hat{\mathbf{a}}_0^{(n)} = \hat{\mathbf{a}}_0^{(n-1)} \hat{\mathbf{u}}(\boldsymbol{x},t)$.

For modeling moving geometries, we define the homogenized velocity $\hat{\boldsymbol{u}}$ as a convex combination of the fluid velocity moment $\boldsymbol{u}$ and the solid velocity $\boldsymbol{u}^{\mathrm{B}}$, given by

$$\hat{\boldsymbol{u}}(\boldsymbol{x},t) = d(\boldsymbol{x},t)\boldsymbol{u}(\boldsymbol{x},t) + (1-d(\boldsymbol{x},t))\boldsymbol{u}^{\mathrm{B}}(\boldsymbol{x},t), \tag{11}$$

where $d(\boldsymbol{x},t)$ is the so-called lattice porosity

$$d(\boldsymbol{x},t) = 1 - \frac{\triangle x^2 \nu_{\mathrm{mo}} \tau_{\mathrm{mo}}}{K(\boldsymbol{x},t)} \in [0,1]. \tag{12}$$

for given local permeabilities $K(\boldsymbol{x},t)$ and molecular relaxation time τ_{mo}. Being computed from these parameters, the lattice porosity is strictly grid-dependent. As such, rigorously connecting it to a macroscopic solid geometry is challenging [40]. For this reason, rather than representing a physical homogenization of the vocal fold tissue, this mapping is utilized strictly as a numerical volume penalization. By driving the permeability $K \to 0$ inside the solid domain, the HLBM acts as a Brinkman-penalization solver that recovers the Navier–Stokes equations with no-slip boundary conditions in the limit. The macroscopic penalization limits map directly to the discrete lattice porosities: the fully fluid limit $K \to \infty$ corresponds to $d = 1$, while the solid penalization limit $K \xrightarrow{\triangle x \to 0} 0$ corresponds to $d = 0$. To ensure a non-slip boundary condition on the moving solid surface, $\boldsymbol{u}^{\mathrm{B}}$ must be set to the velocity of the solid surface. Otherwise, momentum is not transferred from the solid. Connecting the HRRLBM (5) to the FBNSE (1) target equation, a second-order approximation in space for the fluid velocity moment [37,41] can be expected.

The HRRLBM (5) collision step is implemented in the open-source LBM framework OpenLB [34], Version 1.8 [35]. Analogously to all other employed models (cf. Section 2.3), it is expressed as a dynamics tuple, a *domain specific language* (DSL) for local LB cell models. Listing 1 shows how the model is constructed in the DSL a tuple of moment system, equilibrium, and collision operator. Due to this abstract implementation of the LB models against the *concept of a cell* [36,42], they can not only be transparently executed both on CPUs and GPUs but are also amenable to automatic code optimization using common subexpression elimination (CSE). The performance impact of this optimization is discussed in Section 3.1.

Listing 1 Dynamics tuple formulation of the HRRLBM scheme

```
using HRRLBM = dynamics::Tuple<
  float, descriptors::D3Q19<>,                                        ▷ Value type and lattice stencil
  typename momenta::Tuple<                                                ▷ Macroscopic moment system
    momenta::BulkDensity,
    momenta::MovingPorousMomentumCombination<momenta::BulkMomentum>,                     ▷ Eq. (11)
    momenta::BulkStress,
    momenta::DefineToNEq
  >,
  equilibria::ThirdOrder,                                                 ▷ Equilibrium distribution
  collision::ParameterFromCell<                                         ▷ Modified collision operator
    collision::LES::SMAGORINSKY,
    collision::SmagorinskyEffectiveOmega<collision::ThirdOrderRLB>>
>;
```

2.1.3. Representation of deforming VFs

A core methodological contribution of the proposed FSI solver is the mechanism used to map the discrete structural dynamics of the 6MM into the Eulerian grid of the fluid solver without expensive remeshing. In the present work, we use the FBNSE (cf. Eq. (1)) realized via (H)RRLBM for the whole simulation domain except the outer boundary conditions. This allows incorporation of the full dynamics of the VF model without remeshing if we can represent it as a time-dependent porosity field.

For the established usage of HLBM in resolved particulate flows [30,31] as well as more recent use in wall-modeled rotor flows [32], this is approached by considering the lattice porosity as a function

$$d(\mathbf{x},t) := \begin{cases} 0 & \text{if } \phi(\mathbf{x},t) \leq -\frac{\epsilon_h}{2} \\ s(\phi(\mathbf{x},t)) & \text{if } \phi(\mathbf{x},t) \in (-\frac{\epsilon_h}{2}, \frac{\epsilon_h}{2}) \\ 1 & \text{if } \phi(\mathbf{x},t) \geq \frac{\epsilon_h}{2} \end{cases} \tag{13}$$

of the signed distance $\phi(\mathbf{x},t)$ to the solid surface with transition width $\epsilon_h = \epsilon \triangle x$ and transition function $s : \mathbb{R} \to [0,1]$. A common choice for the transition function s is

$$s(\phi) = \frac{\phi}{\epsilon_h} + \frac{1}{2}, \tag{14}$$

s.t. the *real* solid wall is the level set of $d(\mathbf{x},t) = 1/2$ (cf. [30, Fig. 2], Figs. 3 and 4). Because we directly couple the transition width to the grid resolution ($\epsilon_h = \triangle x$), the fluid-solid interface spans a single lattice cell. At this discrete resolution, higher-order profiles cannot be accurately represented and offer no numerical advantage over a linear formulation. While this sharp, single-cell transition introduces a $\mathcal{O}(\epsilon_h)$ truncation error and spurious momentum leakage near the interface, it is an acceptable compromise. The 6MM structural dynamics are driven by macroscopic, subcycle-averaged pressure differences, rendering the global cycle insensitive to localized sub-grid momentum leakage.

Updating the porosities due to an element's displacement or shape change can be implemented efficiently without re-checking all cells due to boundary movement necessarily being bounded by the lattice speed of sound. That is, between each discrete time step, the surface of the VF may only displace less than the distance between adjacent cells at the characteristic lattice velocity. Due to this, the distance to surface and any state change only needs to be computed at the solid frontier surrounded by a *growth layer* (cf. orange cells in Fig. 3).

For the present application, we voxelize a triangulated *master*-fold geometry, linearly covering all variations between maximal convergence, resp. divergence in a separate inertial reference grid. As shown in Fig. 4, slices of the reference grid are embedded into HLBM lattice porosities for given offsets at every discrete timestep. Each per-cell porosity value is associated with an integer *tag*, which connects it to its specific slice.

This approach is implemented in OpenLB [34] as platform-transparent operators [36,42]. Slice selection is implemented in a modified version of the `ReferenceLatticePorosityF` FSI element, allowing parameterization of individual slices of the VF by specifying only a slice offset and the lateral displacement relative to the glottal midline. This *structure response* is obtained via the preCICE [43] interface from the structural model (cf. Section 2.2). The *fluid response* transmitted to the solid side consists of the pressure difference between two reference points m_1 and m_2 sampled at every time step. An overview of the complete time loop from the LBM-solver perspective is given in Listing 2.

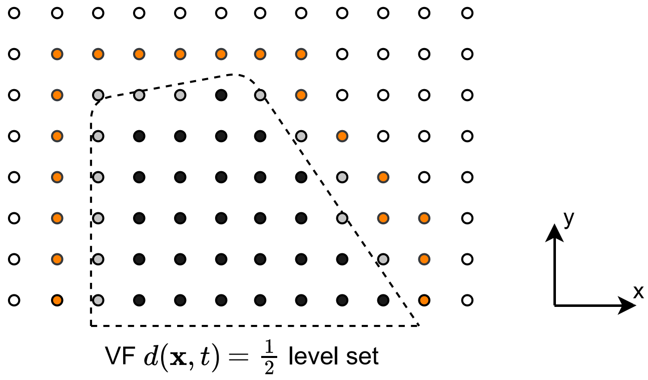

Fig. 3. Context for the efficient local update of porosities from signed distance geometry. Dashed line marks the VF level set $d(\mathbf{x},t) = {}^1\!/_2$ (equivalent to $\phi(\mathbf{x},t) = 0$ by Eq. (13)), black cells are fully in the solid ($d(\mathbf{x},t) = 0$), shaded gray cells are at the solid frontier ($d(\mathbf{x},t) \in (0,1)$) and orange cells mark the fully-fluid growth layer. White cells are fully-fluid ($d(\mathbf{x},t) = 1$) and separated by at least one cell from the FSI region. (For interpretation of the references to color in this figure legend, the reader is referred to the web version of this article.)

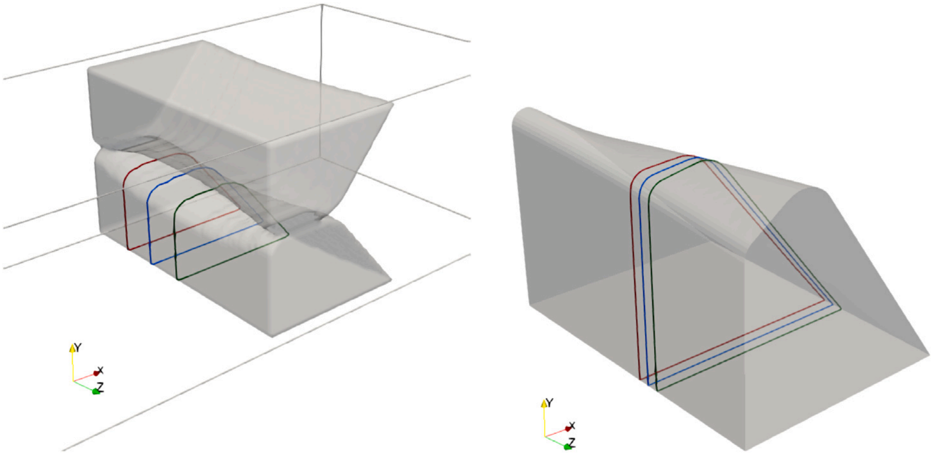

(a) Porosity level set $d(\mathbf{x},\cdot) = {}^1\!/_2$, embedded into the LBM simulation domain as different slices of the reference geometry.

(b) Reference geometry for all fold surface configurations between max. convergent resp. divergent (cf. Fig. 6).

Fig. 4. Representation of deformable VFs as slices of a reference geometry. Colored lines mark exemplary fold surface slices in the LBM simulation and their corresponding location in the reference geometry. (For interpretation of the references to color in this figure legend, the reader is referred to the web version of this article.)

2.2. Six-mass model (6MM)

To represent VF oscillations, each fold is modeled by six lumped masses arranged along the medial surface: three at the inferior-medial edge and three at the superior-medial edge, uniformly spaced in the *anterior–posterior* direction (see Fig. 5). Following [44], the masses move only in lateral direction (along $\hat{x}$, see Fig. 5). The anterior and posterior endpoints serve as fixed anchors for the reconstruction of the continuous medial contour.

For notational clarity, we index the fold side by $q \in \{L, R\}$ (left/right), the row of the masses by $s \in \{1, 2\}$ (upper/lower mass), and the anterior–posterior position by $i \in \{1, 2, 3\}$. The equations of motion for each point mass read

$$\begin{cases} \dfrac{dx_{q,s,i}}{dt}(t) = v_{q,s,i}(t), \\ [t]m_{s,i}\dfrac{dv_{q,s,i}}{dt}(t) = F^a_{q,s,i}(x,v) + F^v_{q,s,i}(x) + F^l_{q,s,i}(x) \\ \qquad\qquad + F^c_{q,s,i}(x) + \delta_{s1}F^d_{q,s,i}(p,x) \end{cases} \tag{15}$$

where F^a are anchor (spring–damper) forces, F^v are vertical coupling forces between upper and lower rows, F^ℓ are longitudinal (anterior–posterior) coupling forces between adjacent masses, F^c are collision/contact forces between the left and right folds, and

Listing 2 Time-loop of the two-way coupled LBM-6MM FSI

```
while simulation time < max simulation time do
    $\mathbf{d}_Y, \mathbf{d}_S, \mathbf{v} \leftarrow$ preCICE.readData("Y", "Slice", "Velocity")
    for each VF slice $i$ do
        $\mathbf{pos} \leftarrow$ GetSlicePosition($\mathbf{d}_Y[i]$)      ▷ Relate 6MM slice position to LBM
        $d_S \leftarrow$ GetSlice($\mathbf{d}_S[i]$)      ▷ Relate 6MM slice surface to master offset
        $\mathbf{u} \leftarrow \{0, \mathbf{v}[i], 0\}$      ▷ Surface velocity
        UpdateElement(i, $\mathbf{pos}, d_S, \mathbf{u}$)
    UpdatePorosityEmbeddingO      ▷ Applies update to porosity field
    $p_{m1} \leftarrow 0,\ p_{m2} \leftarrow 0$      ▷ Reset pressure measurements
    for $i = 1$ to $N_{\text{substeps}}$ do      ▷ Fluid solver sub-cycling
        SetBoundaryValues
        CollideAndStream      ▷ Usual (H)RRLBM timestep
        $p_{m1} \leftarrow p_{m1} +$ SamplePressureAt($m_1$)
        $p_{m2} \leftarrow p_{m2} +$ SamplePressureAt($m_2$)
    $p_{m1} \leftarrow p_{m1} / N_{\text{substeps}}$
    $p_{m2} \leftarrow p_{m2} / N_{\text{substeps}}$
    $\Delta p \leftarrow p_{m1}^{\text{global}} - p_{m2}^{\text{global}}$
    preCICE.writeData("Pressure", $\Delta p$)
    preCICE.advance($\Delta t_{\text{coupling}}$)
```

F^d are fluid-induced driving forces. Unlike previous implementations, F^d couples the 6MM to the HLBM fluid solver, enabling fully two-way FSI (cf. Section 2.1.3). Unlike to previous implementations [44], the actual and local fluid-pressure-forces at every coupling step are transferred to the inferior masses of the 6MM during the entire oscillation cycle. Thus, the pressure profile along the vocal fold (i.e. along the line of inferior masses of each vocal fold) is reflected. In contrast, the inferior–superior pressure distribution along the glottal duct cannot be captured by the basic design of the 6MM. A further limitation of the 6MM is the lack of transferring viscous stresses onto the vocal fold surface which supports the mucosal wave formation.

To reflect the near-linear stiffness at small strains and the exponential stiffening at larger deformations [47–49], we employ a displacement-dependent stiffness [50,51]:

$$\tilde{k}_{s,i} \;=\; k_{s,i}\left(1 + \xi\, x_{q,s,i}^2\right), \qquad \xi = 100\,\text{cm}^{-2}, \tag{16}$$

which replaces the nominal $k_{s,i}$ in F^a and prevents unrealistically large amplitudes at elevated subglottal pressures [1].

We emphasize that the collision force F^c is purely enforced through linear penalty springs. As the VFs are represented as a porosity field within the fluid solver, the HLBM does not fully resolve the thin-film fluid dynamics (squeeze-film effect) in the microscopic gap immediately preceding total closure. Consequently, the contact mechanics rely on the 6MM penalty formulation rather than a fluid-resolved cushioning mechanism.

2.2.1. *Mucosal wave and elliptic glottis*

The vertical coupling between superior and inferior rows of mass points produces the characteristic mucosal wave characterized by the associated convergent–divergent glottal shape change of the glottal duct during an oscillation cycle (Fig. 6). Based on the M5 geometry, the maximum convergent configuration is defined when the superior-medial edge of the medial surface is displaced by $+1.5\,\text{mm}$ and the inferior edge by $-1.5\,\text{mm}$; the maximum divergent configuration inverts these displacements. The difference between these limiting states quantifies the degree of convergence/divergence of the glottal duct formed by the medial surfaces during the oscillation cycle.

After time integration of Eq. (15), the discrete displacements are converted into a smooth medial contour by a cubic spline along the glottis axis, using the anterior and posterior endpoints as fixed anchors. In each coronal plane, the glottal cross-section is then reconstructed as an ellipse parametrized by the interpolated medial edge positions, yielding the characteristic elliptical shape of the glottis [1]. To summarize, the convergent and divergent positions of the VFs are achieved by allowing the upper and lower masses to move by $\pm 1.5\,\text{mm}$ each, see Fig. 6. In addition, the entire vocal fold slice can be globally displaced within the domain in the y-direction by $\pm 3\,\text{mm}$, see Fig. 7.

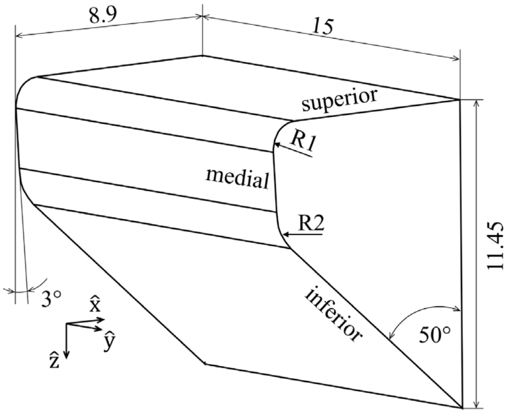

(a) Three-dimensional representation of a single VF based on the M5 model [45,46], illustrating the key geometric dimensions and a glottal angle of 3°. The figure highlights the superior, medial, and inferior surfaces, providing the anatomical boundaries used for modeling and analysis.

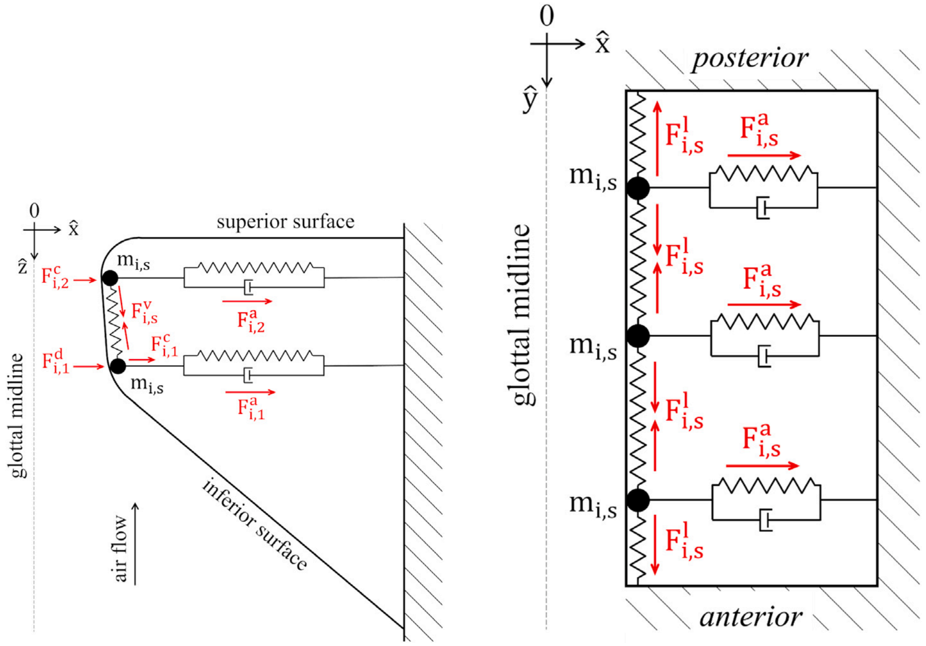

(b) Coronal view showing representative masses $m_{q,s,i}$ at the inferior- and superior-medial edges. Springs/dampers generate anchor forces $F^a_{q,s,i}$, vertical couplings $F^v_{q,s,i}$, and collision forces $F^c_{q,s,i}$. The driving force $F^d_{q,s,i}$ acts laterally ($\hat{x}$) on the inferior row.

(c) Superior view with three equally spaced point masses along the AP axis for each row; longitudinal springs/dampers provide coupling in $\hat{y}$.

Fig. 5. Schematic of the six-mass vocal-fold model.

2.3. Simulation setup and FSI coupling

We simulate the airflow in a three-dimensional laryngeal channel. The vocal-fold geometry follows the M5 template with a glottal half-angle of 3° and clearly defined superior, medial, and inferior surfaces (see Fig. 5(a)) specified in the benchmark case defined by Schoder et al. [8]. The fold is embedded in a rectangular computational domain of size $L_x \times L_y \times L_z$ which is shown in Fig. 7. Unless stated otherwise, the medial plane of the glottis coincides with the x–y mid-plane.

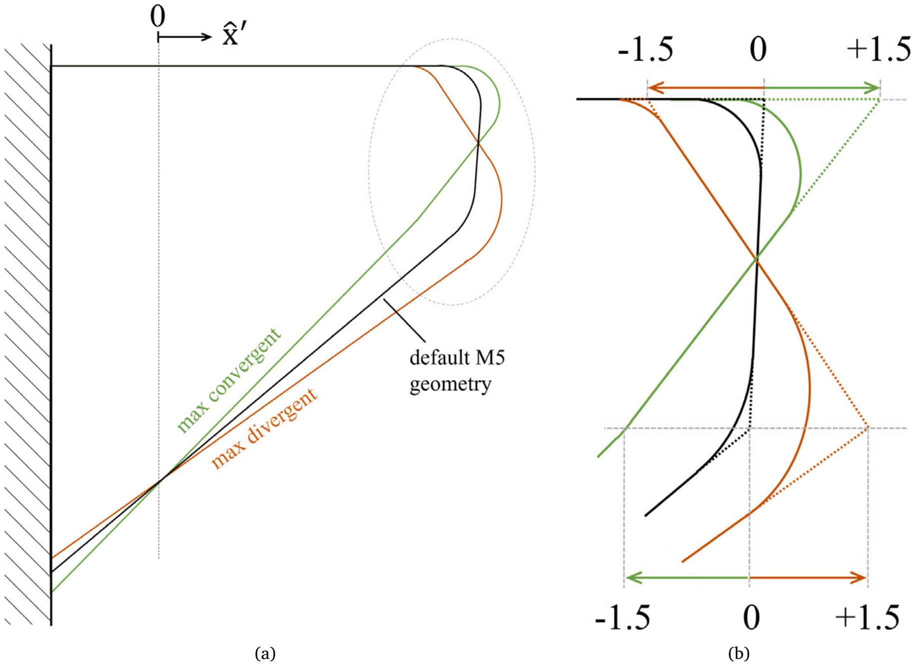

Fig. 6. Convergent (green) and divergent (orange) phases within one oscillation cycle as computed by the 6MM. (a) maximum trajectories of the medial edges in $\hat{x}'$ showing the out-of-phase motion of inferior and superior rows. (a) schematic with maximum medial displacement (horizontal) and vertical offset (vertical). Coordinates are scaled to visualize a ±3 mm shift around the glottal midline. See also Fig. 4(b). (For interpretation of the references to color in this figure legend, the reader is referred to the web version of this article.)

Table 1
Parameters of the LBM simulation.

Parameter	Description	Value
L_x	Streamwise domain extent	0.1 m
L_y	Vertical domain extent	0.01 m
L_z	Spanwise domain extent	0.015 m
L_f	Streamwise leading edge of the fold	0.012 m
m_1	Pressure sampling position 1	[0.0875 m, 0.0052 m, 0.0075 m]
m_2	Pressure sampling position 2	[0.082 m, 0.0052 m, 0.0075 m]
L_{char}	Characteristic length	0.001 m
N	Resolution factor	5
δx	Spatial voxel size	2×10^{-4} m
δt_{f}	Discrete time step	8.63547×10^{-7} s
ρ	Fluid density	1.293 kg/m^3
ν	Kinematic viscosity	1.544×10^{-5} m^2/s

This domain is discretized on a uniform Cartesian grid with parameters given in Table 1, yielding a total cell count of approx. 2×10^6. At the inflow, the reference pressure is enforced using a local pressure condition while the outflow is smoothly ramped up to $1\,\text{m}\,\text{s}^{-1}$ over 0.01 s. Stability at the inflow is ensured by applying a fringe zone. A no-slip condition is applied to all outer walls using standard full-way bounce back.

Two-way coupling between fluid and structure is realized via preCICE [43], acting as a communication and coordination layer between the C++-based fluid solver and the Python-based structure solver.

Forces and displacements are exchanged every $\Delta t_{\text{c}} = 1.38 \times 10^{-5}$ s, while the fluid solver advances with sub-cycling at $\Delta t_{\text{f}} = 8.63547 \times 10^{-7}$ (see Table 1). At each coupling step, the subcycle-averaged pressure at the two reference sample points is mapped to the three inferior control points per VF, where it acts as the lateral driving force $F^d_{q,1,i}$. The 6MM is implemented in Python and integrated with a classical fourth-order Runge–Kutta scheme, analogously to [44]. Table 2 lists the nominal parameters used for the 6MM. Symmetric VFs are assumed, i.e., identical properties are used for left and right fold. The updated displacements of both upper and lower row of masses are communicated back to the OpenLB flow solver, which updates the moving boundary slices accordingly. This procedure yields a stable, fully explicit two-way FSI coupling, capturing the mutual interaction of airflow and VF motion.

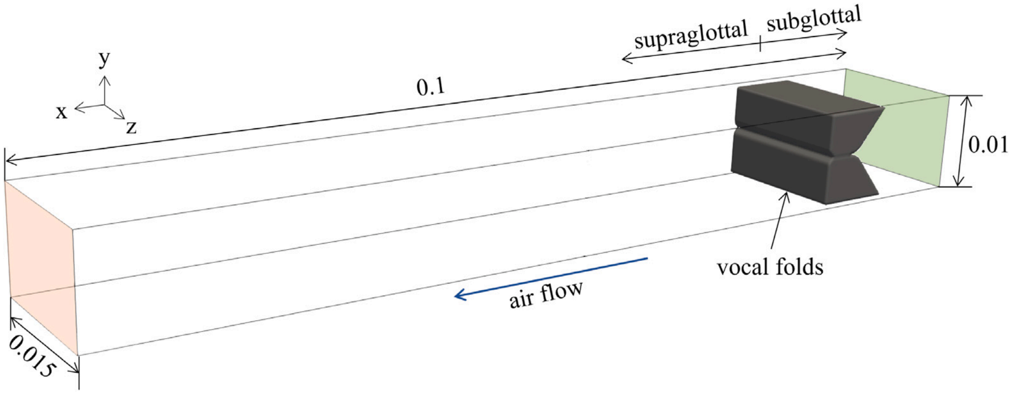

Fig. 7. Setup of the LBM simulation domain with VF geometry represented as porosity level set $d(x,0) = 1/2$. Pressure inflow shaded in green and velocity outflow in red. (For interpretation of the references to color in this figure legend, the reader is referred to the web version of this article.)

Table 2
Nominal initial values and standard parameters for the six-mass model (6MM). Unless noted otherwise, values are reported in cm, g, and ms. Index $s = 1$ denotes lower masses, $s = 2$ upper masses. For the baseline configuration, $\alpha_m = \alpha_k = 4$ was chosen for the masses and the spring stiffnesses.

Parameter	Description	Value
$m_{i,1}$	Lower mass	$0.04166 \times \alpha_m$
$m_{i,2}$	Upper mass	$0.004166 \times \alpha_m$
$k_{i,1}$	Lower anchor stiffness	$0.34666/\alpha_k$
$k_{i,2}$	Upper anchor stiffness	$0.034666/\alpha_k$
k_b^v	Vertical spring stiffness	2.5
$k_{i,s}^\ell$	Longitudinal spring stiffness	–
$r_{i,1}$	Lower damping coefficient	0.0666
$r_{i,2}$	Upper damping coefficient	0.0666
$k_{i,1}^c$	Lower collision stiffness	$3k_{s,1}$
$k_{i,2}^c$	Upper collision stiffness	$3k_{s,2}$
$x_{i,1}^r$	Rest position lower mass	0.0175
$x_{i,2}^r$	Rest position upper mass	0.0175
d	Thickness of masses	8.9
ℓ	Glottal length	1.5

2.4. Data analysis

Flow fields are asynchronously exported by OpenLB in VTK format [52] and post-processed in ParaView [53,54] to enable use of an existing in-house analysis software. Three probes in the supraglottal region are defined where the velocity magnitude is sampled at identical x and y but different spanwise positions ($z/L_z = 0.5$): $x = 0.08\,\text{m}$, $y = 0.052\,\text{m}$, $z = 0.0075\,\text{m}$ (50% span).

The flow parameters are sampled at $f_s = 10\,\text{kHz}$. A subglottal pressure probe at $x = 0.095\,\text{m}$, $y = 0.052\,\text{m}$, $z = 0.0075\,\text{m}$ records the time-varying subglottal pressure $p_{\text{sub}}(t)$; unless specified otherwise, the reported subglottal pressure corresponds to its time mean $\overline{p}_{\text{sub}}$.

Using an in-house analysis software, the Glottis Analysis Tools [55] (GAT, University Hospital Erlangen, Erlangen, Germany), we extract standard glottal dynamics metrics, including the Glottal Gap Index (GGI) [56], Opening Quotient (OQ) [57], Closing Quotient (ClQ) [58], Amplitude Symmetry Index (ASI) [59], Phase Asymmetry Index (PAI) [56], Time Periodicity (TP) [60], Amplitude Periodicity (AP) [60] and the fundamental frequency f_0 from the oscillating VFs, using 25 consecutive VF oscillation cycles to ensure stable parameter computation.

3. Results and discussion

3.1. Coupling verification and performance

In order to determine the sensitivity of the coupled solver to the time step, we varied the HLBM-6MM coupling interval over nearly two orders of magnitude, $\Delta t_c \in \{8.64 \times 10^{-7}, 1.73 \times 10^{-6}, 3.45 \times 10^{-6}, 6.91 \times 10^{-6}, 1.38 \times 10^{-5}\}$ s, and evaluated standard glottal metrics. All tests used the baseline six-mass configuration with the mass and stiffness scaling set to $\alpha_m = \alpha_k = 4$ (see Table 2, where masses scale with α_m and anchor stiffnesses with $1/\alpha_k$); unless stated otherwise, the values we report below – particularly f_0 and

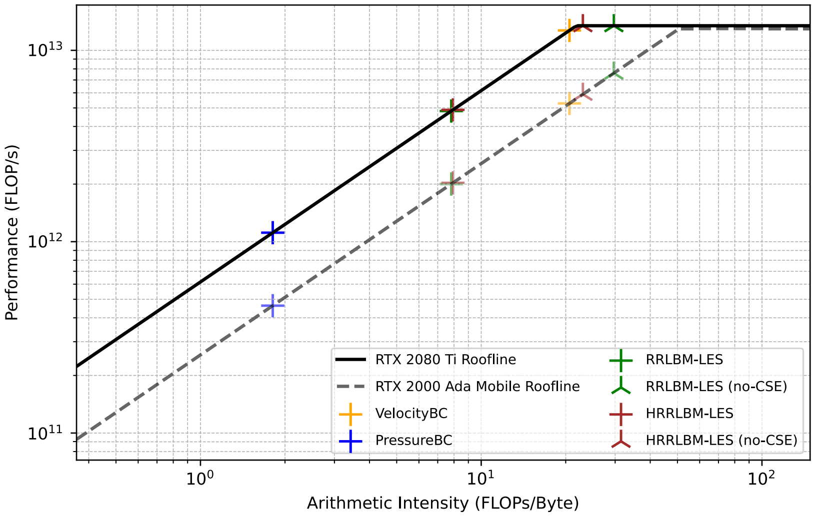

Fig. 8. Theoretical roofline analysis of all used LBM collision operators. For the two bulk models (H)RRLBM both optimized and unoptimized versions are shown to illustrate the impact of common subexpression elimination. Rooflines for both GPUs are based on theoretical *floating point operations per second* (FLOP/s) and bandwidth values of the manufacturer (NVIDIA RTX 2080 Ti: 1.345×10^{13} FLOP/s, $616\,\mathrm{GB\,s^{-1}}$; RTX 2000 Ada Mobile: 1.299×10^{13} FLOP/s, $256\,\mathrm{GB\,s^{-1}}$).

the glottal parameters – refer to this configuration. Across this sweep the fundamental frequency remained essentially unchanged (range 247–249 Hz; variation $< 0.8\%$), complete closure was preserved in every case (GGI = 0), symmetry of the glottis shape stayed high (ASI = 0.98–0.99, PAI ≤ 0.01), and the open/close fractions changed only slightly (OQ = 0.63–0.65, ClQ = 0.29–0.32; absolute differences ≤ 0.026). These results indicate that the limit cycle and its key kinematic signatures are robust to Δt_c within the tested range.

We also recorded wall-clock cost per oscillation cycle (RTX 2080 Ti): 20.7, 12.1, 13.7, 8.61, and 8.68 min for the coupling steps listed above. Although the cost is not strictly monotonic (likely due to the coupling complexity), the two largest intervals provide a ∼2.4× speedup versus the smallest interval while maintaining the same metrics. This observation is also backed by the roofline analysis of the involved models in Fig. 8, where the compute-optimized collision kernels are bound by the memory bandwidth for both target GPUs.

Together, this points towards the bottleneck not being the time spent in LBM but in the structure model and preCICE coupling. For all production runs, we therefore chose $\Delta t_\mathrm{c} = 6.91 \times 10^{-6}$ s as a pragmatic compromise between accuracy and throughput (about 7 cycles per hour on the comparably old RTX 2080 Ti, 60 cycles per hour on a more recent RTX 2000 Ada mobile GPU); all statistics reported below are computed from at least 25 consecutive cycles of that stable limit cycle.

3.2. General characteristics of FSI

We analyze the default configuration with a constant *pressure inlet* of 800 Pa and a *velocity outlet* of $1\,\mathrm{m\,s^{-1}}$. After a short transient state, the coupled system settles into a periodic stable VF oscillation.

The subglottal pressure time series fluctuates quasi-periodically around $\overline{p}_\mathrm{sub} = 1012.8 \pm 18.8$ Pa, consistent with sustained self-oscillation. The fundamental frequency extracted from the *glottal area waveform* (GAW) is $f_0 = 248 \pm 3$ Hz; the value inferred independently from $p_\mathrm{sub}(t)$ agrees closely, confirming dynamical consistency between structure and flow.

Because the outlet boundary condition prescribes the plane-averaged outlet speed, the outlet *flow rate* is fixed at

$$Q_\mathrm{out} = 1.5 \times 10^{-4}\ \mathrm{m^3\,s^{-1}}\ (\approx 9\ \mathrm{L\,min^{-1}}).$$

Pulsatility is therefore characterized by *supraglottal jet velocities* and *glottal area dynamics* rather than by a fluctuating flow rate at the outlet.

The default configuration operates at a physiologically plausible mean subglottal pressure ($\overline{p}_\mathrm{sub} \approx 1.01$ kPa) and fundamental frequency in the range of typical female phonation ($f_0 \approx 250$ Hz). The imposed velocity outlet fixes the plane-integrated outflow ($Q_\mathrm{out} = 9\ \mathrm{L\,min^{-1}}$), so the cycle-mean inflow matches this value by mass conservation in the periodic state.

Peak jet speeds of $11\,\mathrm{m\,s^{-1}}$ to $12\,\mathrm{m\,s^{-1}}$ are somewhat lower than in some simulation studies [19,25,61,62] that use higher driving pressures or pressure outlets. Two factors likely contribute here: (i) the velocity outlet caps the global volumetric outflow and damps the amplitude of flow-rate excursions, and (ii) the idealized rectangular channel lacks additional constrictions that can locally amplify the jet, as e.g., shown for the constriction between the ventricular folds [63–65]. Importantly, the *cycle-mean* mass flow (∼9 $\mathrm{L\,min^{-1}}$) is realistic for comfortable phonation and therefore consistent with the physiological flow conditions *in vivo*.

3.3. *Glottal parameters, stiffness, and contact*

Cycle-resolved glottal metrics indicate a physiologically plausible open-time bias with reliable complete closure: Across $n = 25$ consecutive cycles, the opening and closing fractions were $\mathrm{OQ} = 0.64 \pm 0.01$ and $\mathrm{ClQ} = 0.30 \pm 0.01$, respectively; the glottal gap index was $\mathrm{GGI} = 0.00 \pm 0.00$, indicating complete closure in every cycle. The oscillation was nearly symmetric, with an amplitude symmetry index of $\mathrm{ASI} = 0.99 \pm 0.00$ and a phase asymmetry index of $\mathrm{ASI} = 0.00 \pm 0.00$. Peak lateral excursions of the medial edge are $A_L = 1.689$ mm (amplitude of the left VF) and $A_R = 1.700$ mm (amplitude of the right VF), yielding a bilateral peak-to-peak glottal width change of 3.389 mm. Cycle-regularity measures are close to unity ($\mathrm{AP} = 0.99 \pm 0.00$, $\mathrm{TP} = 0.99 \pm 0.01$). The effective stiffness parameter used in the 6MM averages $\mathtt{Stiff} = 1390.0 \pm 56.7$

All glottal metrics (OQ, ClQ, GGI, ASI, PAI, AP/TP) are consistent with healthy, stable modal phonation [66,67]: we observe a pronounced open-time bias ($\mathrm{OQ} \approx 0.64$), reliable complete closure ($\mathrm{GGI} = 0$ each cycle), near-symmetry between the folds, and regular cycles. The model reproduces full glottal closure without numerical leakages owing to the geometric reconstruction (spline along anterior–posterior direction and elliptic section with a limited global offset), which is crucial for capturing contact dynamics.

Contact forces were computed separately for each VF and have opposite signs by convention. For a single bilateral contact metric, we report the *average compressive magnitude*,

$$F^c = \tfrac{1}{2}\left(|F^c_{\mathrm{left}}| + |F^c_{\mathrm{right}}|\right) = 27.1 \text{ mN}. \tag{17}$$

which corresponds to an equivalent line load of $q_{c,\mathrm{peak}} \approx 1.80\ \mathrm{N\,m^{-1}}$ when normalized by glottal length ($\ell = 15$ mm). This avoids double-counting while remaining comparable across cases.

The peak bilateral contact force of $F^c \approx 27.1$ mN falls within *in vivo* ranges reported by Gunter et al. [68] (5–42 mN), while exceeding values measured on excised larynges at very low subglottal load reported by Lagier et al. [69] (0.7–12 mN at ∼0.2 kPa). This is expected because our default configuration operates at a higher driving pressure (∼1 kPa) and achieves complete closure. Overall, the contact forces are physiologically credible in magnitude and timing (coinciding with GGI = 0).

3.4. *Supraglottal jet signatures*

Velocity probes 50% span show strongly pulsatile jet with *cycle-to-cycle peaks* of 11–12 $\mathrm{m\,s^{-1}}$ and indicating a largely coherent jet for the symmetric baseline configuration. Velocity maxima coincide with maximal glottal opening, and minima occur during the closing phase.

Fig. 9 displays one representative oscillation cycle in the mid-coronal plane, showing the glottal duct shape, velocity magnitude, and subglottal pressure field. The subfigures are arranged *from top to bottom* as *closed → opening → complete open → closing → closed*.

Starting with the time point (1) with the closed glottis, the supraglottal flow still exhibits the trace of the glottal jet of the previous oscillation cycle with a slight pressure difference between subglottal and supraglottal region. By increasing the subglottal pressure in time point (2), the glottis opens and the flow velocity between the VFs increases and the intraglottal pressure drops. This opening process of the glottis is supported by the decreasing pressure level in the supraglottal tract due to the inertia of the air bulk which is modeled by the constant outflow boundary condition farther downstream. The further opening motion of the VFs in time point (3) allows the intraglottal flow to further accelerate to its maximum velocity of $12\,\mathrm{m\,s^{-1}}$ entering almost the supraglottal flow duct. As a consequence, the static pressure starts to increase in the supraglottal channel due to the displacement of the previously decelerating supraglottal air bulk volume. The largest opening of the glottal gap is reached in time point (4) which marks the start of the closing motion of the VFs. At this time, the sub-/supraglottal pressure difference is very small. During the closing motion, two vortices at the tip of the glottal jet build up and the static pressure in the supraglottal region becomes maximal in time point (5). Shortly before the glottis closes in time point (6), the flow is interrupted with a small pressure peak in the very narrow gap between VFs whereas the supraglottal pressure further decreases. The following time point (7) corresponds to time point (1) with increasing contact force between the VFs with a maximum of 27.1N as described above. In time points (1), (3) and (7), the transverse velocity plane (2nd column from left in Fig. 9) shows a double-jet structure as reported by Michaud-Dorko et al. [70] who measured the 3D flow field in the supraglottal region of a synthetic larynx model. As difference, they reported much smaller oscillation frequencies around $125\ \mathrm{Hz}$ and a much higher max. flow velocity of approx. $50\ \mathrm{m/s}$. Despite these deviations, the process simulated here shows the characteristic flow features as widely reported in other studies with computational as well as experimental larynx models [3,21]. A direct comparison with experimental data is not possible, because the lumped-mass model of the vocal folds cannot be reproduced experimentally. However, the basic parameters of the flow field and the their oscillations as well as the basic flow field topology show the characteristic structures as described above.

3.5. *Parameter variation of the lumped-mass model*

To analyze the influence of the mass and the spring constants, they were varied according to their definition in Table 2. Thus, the mass and spring constant were scaled relative to the baseline case with $\alpha_m = \alpha_k = 4$ denoted as `m40k40`):

$$m_{i,s} = \alpha_m\, m^{(0)}_{i,s}, \qquad k_{i,s} = k^{(0)}_{i,s}/\alpha_k, \quad \alpha_m, \alpha_k \in \{3.5, 4.0, 4.5\}. \tag{18}$$

Note that larger α_k implies a lower stiffness. In total, nine combinations of $\alpha_m \alpha_k$ arise. Table 3 shows all combinations and the resulting mean fundamental frequencies and amplitudes averaged over at least 25 consecutive oscillation cycles.

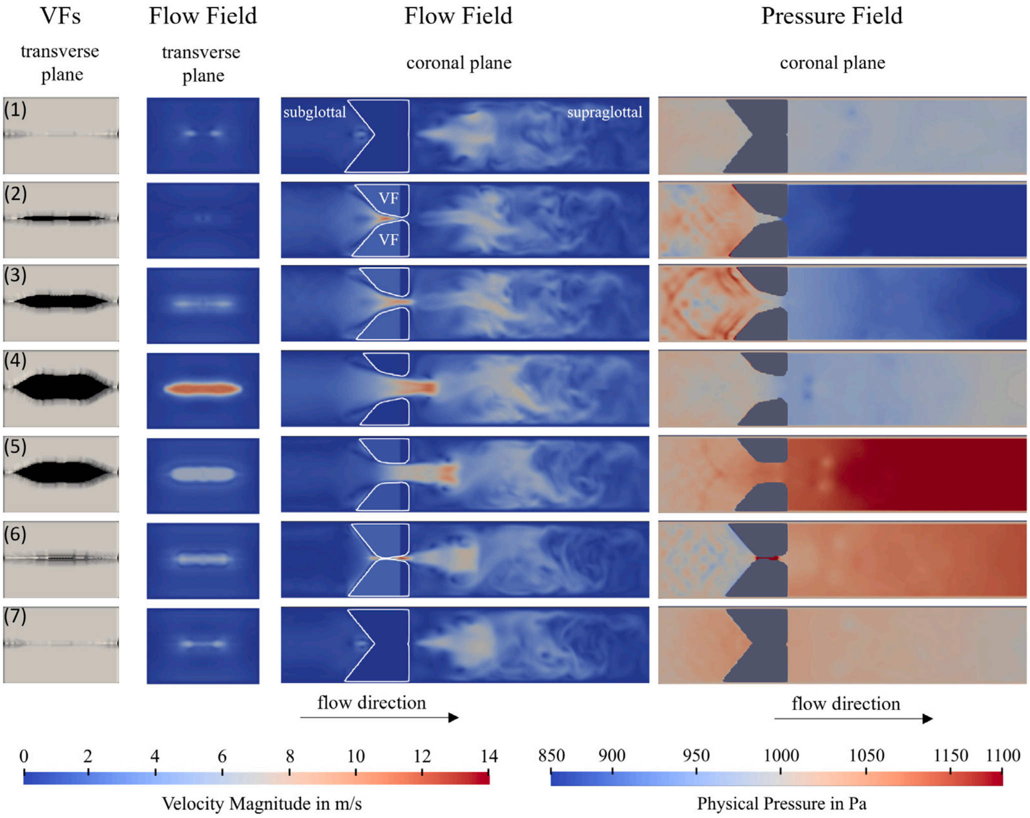

Fig. 9. Visualization of flow field and vocal folds' motion during one oscillation cycle with 7 time points from top to bottom. From left to right: transverse perspective of medial VF; transverse plane with velocity magnitude approx. 0.65 mm downstream of the vocal folds; mid-coronal plane with velocity magnitude; mid-coronal plane with static pressure. Convergent opening, divergent post-peak with intraglottal vortex formation, and late-closing phases are shown from top to bottom.

Table 3
Fundamental frequency for mass–spring scalings (α_m, α_k); values are mean ± SD over ≥ 25 consecutive cycles. Reference case: `m40k40`.

Case	$\chi = 4/\sqrt{\alpha_m \alpha_k}$	f_0 [Hz]
m35k35	1.1429	260.999 ± 3.213
m35k40	1.0690	256.478 ± 9.802
m35k45	1.0079	251.282 ± 2.617
m40k35	1.0690	252.821 ± 3.248
m40k40	1.0000	248.293 ± 2.794
m40k45	0.9428	245.122 ± 2.489
m45k35	1.0079	246.829 ± 3.109
m45k40	0.9428	242.509 ± 2.531
m45k45	0.8889	239.954 ± 2.765

In accordance, Fig. 10 displays the fundamental frequency and amplitude for the parameter variation. It shows that an increasing mass (i.e. increasing α_m) and a decreasing stiffness (i.e. increasing α_k) both produce an amplitude rise (Fig. 10(a) and a fundamental frequency decay (Fig. 10(b). The oscillation amplitude turned out to be similarly influenced by mass and stiffness variation. In contrast, the fundamental frequency exhibits a slightly larger decay for mass variation as for stiffness.

Across the sweep, the fundamental frequency follows the dimensionless index $\chi = 4/\sqrt{\alpha_m \alpha_k}$: larger χ corresponds to higher f_0, as expected for a one mass–spring oscillator with an eigenfrequency that follows $f_0 \propto 1/\sqrt{\alpha_m \alpha_k}$. Increasing the mass ($\alpha_m \uparrow$) or reducing the stiffness ($\alpha_k \uparrow$) lowers f_0. Iso–χ pairs (m35k40 vs. m40k35; m35k45 vs. m45k35; m40k45 vs. m45k40) yield very similar f_0, with small but systematic offsets (about 2–4 Hz) indicating a slightly stronger influence of mass than stiffness at fixed χ. All frequencies (240 Hz to 261 Hz) remain within a physiologically plausible range for modal phonation.

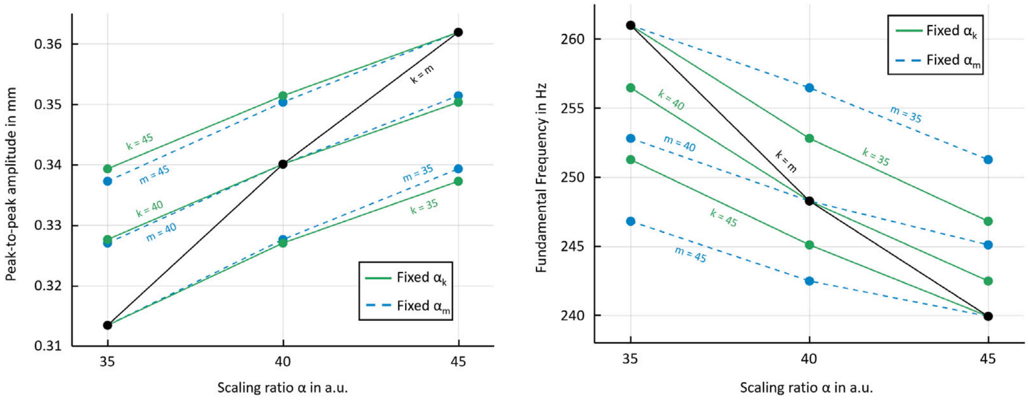

(a) (b)

Fig. 10. Effect of mass and stiffness scaling on VF kinematics and pitch. (a) Relative peak lateral amplitude versus scaling level ($\alpha \in \{3.5, 4.0, 4.5\}$; shown as 35/40/45). Blue dashed lines: fixed α_k (varying α_m); green solid lines: fixed α_m (varying α_k). (b) Fundamental frequency for the same cases. The black diagonal indicates $\alpha_m = \alpha_k$ (synchronous mass-stiffness scaling). Amplitudes rise with increased effective mass or reduced stiffness; f_0 decreases under both changes. Iso–χ pairs ($\alpha_m\alpha_k$ = const.) cluster closely in f_0 with only small, systematic offsets that favor the mass effect. (For interpretation of the references to color in this figure legend, the reader is referred to the web version of this article.)

4. Summary and conclusion

To address the persistent trade-off between computational efficiency and physiological fidelity in phonation modeling, we presented a novel coupling strategy and high-performance workflow for two-way fluid–structure interaction. By efficiently representing an established six-mass vocal fold model (6MM) as a time-dependent porosity field within the homogenized lattice Boltzmann method (HLBM), we bypassed the topological and performance limitations of traditional moving-mesh approaches.

In a rectangular 3D channel capturing the trachea, the larynx and the vocal tract, the method produced a stable, periodic and physiologically plausible oscillation of the VFs at $f_0 \approx 248$ Hz and $\overline{p}_{\text{sub}} \approx 1.01$ kPa with complete glottis closure (GGI= 0), open-time bias (OQ ≈ 0.64), near-symmetry between folds, and coherent and characteristic supraglottal jet flows with peak velocity of 11–12 $\text{m}\,\text{s}^{-1}$. The cycle-resolved flow-structure signatures across opening, closing, and closed phases (Fig. 9) and the measured peak bilateral collision force ($\approx$27 mN) further support physiological credibility.

A study of the coupling interval between HLBM flow solver and 6MM structure model spanning nearly two orders of magnitude confirmed the robustness of the limit cycle. A systematic variation of mass and stiffness confirmed scaling of the fundamental frequency with the dimensionless mass–spring index $\chi = 4/\sqrt{\alpha_m\alpha_k}$. Within the tested range ($\alpha_m, \alpha_k \in \{3.5, 4.0, 4.5\}$), f_0 decreased monotonically with increasing effective mass or decreasing stiffness, consistent with the expected $f_0 \propto 1/\sqrt{\alpha_m\alpha_k}$ relation. Iso–χ pairs yielded nearly identical frequencies with small systematic offsets, indicating a slightly stronger sensitivity to mass than stiffness. All observed frequencies (240 Hz to 261 Hz) remained within a physiologically plausible range for modal phonation, confirming the robustness of the coupled model.

This novel FSI solver enables very fast simulations due to the fluid-part being executed on GPUs using OpenLB. Simulations of the validation case covering one physical second reached a throughput of 60 oscillation cycles per hour on a mobile *NVIDIA RTX 2000 Ada* GPU, demonstrating the practical usability and efficiency of the approach.

Limitations

The described FSI model is based on certain simplifications, especially for the applied lumped-mass model of the vocal folds. The following list summarizes the simplifications described in the main text above:

(i) *VF representation.* The 6MM restricts motion to the lateral direction and uses a simplified, displacement-dependent stiffness; it does not resolve layered tissue anatomy, anisotropy, or frequency-dependent viscoelasticity.
(ii) *Fluid-force transfer:* The fluid forces are transferred to the 6MM only at the six inferior masses, three on each vocal folds. This formulation neglects the inferior–posterior pressure distribution along the glottal duct and only roughly includes the pressure distribution along the vocal folds at the inferior edges.
(iii) *Fluid dynamical shear-stress:* The fluid dynamical shear stress on the vocal fold surfaces is neglected as the model is not designed to capture tangential forces along the vocal fold contour.
(iv) *Contact and geometry.* The glottis shape is reconstructed as ellipses using a cubic interpolation. Viscous friction or detailed frictional contact mechanics are neglected. The channel geometry is idealized as straight rectangular tube with the M5-geometry benchmark as VF shape.

(v) *Boundary conditions.* The pressure-inlet/velocity-outlet choice fixes the plane-averaged outflow to amount to approx. 9 L $\min^{-1}$ and largely preserves $\overline{p}_{\text{sub}}$ across parameter sweeps, which shapes the observed jet amplitudes and may under-represent acoustic loading effects.
(vi) *Scope of the sweep.* Mass-stiffness scalings were explored within ±12.5% around the reference (plus one extended case) and under symmetric folds; the exponents are regime-specific rather than universal.

Outlook

The performance of the proposed FSI model possess large potentials to enable more realistic, even patient-specific simulations of normal and disturbed phonation cases. Therefore, the inherent simplifications needs to be drastically reduced and more realistic methods and procedures needs to be implemented. The following list displays the single steps to improve the model in this context. Thereby the order in the list shows the priority of reasonable next steps in development from the authors' point of view:

(a) **Incorporation of richer tissue mechanics** (layered body-cover, viscoelasticity) and refined contact models using e.g. models of continuum mechanics as finite element methods.
(b) **Coupling of the glottal source to a 3D vocal-tract model** based on MRI imaging to realistically resolve the aerodynamics and to enable the sound modulation processes within a subsequent aero-acoustic simulation for normal vowel production based on aero-acoustic analogies.
(c) **Improvement of the coupling efficiency** and analysis of adaptive resolution to reach longer phonatory tasks and subject-specific calibration.
(d) Extension of parameter studies to **asymmetric/pathological cases** and broader pressure/flow regimes.
(e) **Introduction of compressibility** to assess source-filter interaction and acoustic back-coupling effects highly relevant in e.g. professional singing.

These steps describe the present trends and strengthen physiological fidelity to improve the predictive power for clinical and voice-science applications.

CRediT authorship contribution statement

Adrian Kummerländer: Writing – original draft, Visualization, Validation, Software, Methodology, Investigation, Formal analysis, Data curation, Conceptualization. **Bogac Tur:** Writing – original draft, Visualization, Validation, Software, Methodology, Investigation, Formal analysis, Data curation, Conceptualization. **Maik Haase:** Writing – review & editing, Validation. **Fedor Bukreev:** Writing – review & editing, Methodology. **Michael Döllinger:** Writing – review & editing, Supervision. **Mathias J. Krause:** Writing – review & editing, Supervision, Resources, Funding acquisition. **Stefan Kniesburges:** Writing – review & editing, Supervision, Resources, Funding acquisition.

Adrian Kummerländer and Bogac Tur equally contributed to the manuscript as joint first authors.

Declaration of competing interest

The authors declare that they have no known competing financial interests or personal relationships that could have appeared to influence the work reported in this paper.

Acknowledgments

This work was partially funded by the NHR@KIT Call for Collaboration project "OpenLB – An Open Source High Performance Lattice Boltzmann Code for Heterogeneous CPU–GPU Clusters" as well as Deutsche Forschungsgemeinschaft (DFG), Germany grant number 468824876.

This work has received funding from the European Union's Horizon Europe research and innovation programme under grant agreement No 101138305.

This work was supported by Deutsche Forschungsgemeinschaft (DFG), Germany (Grant Nos DO1247/21-1 and SCHU3441/4-1).

Data availability

Data will be made available on request.

References

[1] I.R. Titze, Principles of Voice Production, second ed., National Center for Voice and Speech, 2000.

[2] R. Mittal, B.D. Erath, M.W. Plesniak, Fluid dynamics of human phonation and speech, Annu. Rev. Fluid Mech. 45 (2013) 437–467, http://dx.doi.org/10.1146/annurev-fluid-011212-140636.

[3] S.L. Thomson, Synthetic, self-oscillating vocal fold models for voice production research, J. Acoust. Soc. Am. 156 (2) (2024) 1283–1308, http://dx.doi.org/10.1121/10.0028267.

[4] M. Semmler, et al., 3D reconstruction of human laryngeal dynamics based on endoscopic high-speed recordings, IEEE Trans. Med. Imaging 35 (7) (2016) 1615–1624, http://dx.doi.org/10.1109/TMI.2016.2521419.

[5] R. Veltrup, et al., Three-dimensional analysis of vocal fold oscillations: Correlating superior and medial surface dynamics using ex vivo human hemilarynges, Bioengineering 11 (10) (2024) http://dx.doi.org/10.3390/bioengineering11100977.

[6] K. Stevens, Acoustic phonetics, in: S.J. Keyser (Ed.), in: Current Studies in Linguistics, vol. 30, The MIT Press, 2000.

[7] J. Wendler, W. Seidner, U. Eysholdt, Lehrbuch der Phoniatrie und Pädaudiologie, fourth, Thieme, Stuttgart, Stuttgart, 2005.

[8] S. Schoder, et al., A benchmark case for aeroacoustic simulations involving fluid-structure-acoustic interaction transferred from the process of human phonation, Acta Acust. 8 (2024) 13.1–13.16, http://dx.doi.org/10.1051/aacus/2024005.

[9] I.R. Titze, B.H. Story, Acoustic interactions of the voice source with the lower vocal tract, J. Acoust. Soc. Am. 101 (4) (1997) 2234–2243, http://dx.doi.org/10.1121/1.418246.

[10] B.H. Story, et al., Detection of synchronization of the voice source and vocal tract in connected speech, J. Acoust. Soc. Am. 158 (3) (2025) 2207–2224, http://dx.doi.org/10.1121/10.0039348.

[11] J.G. Svec, Z. Zhang, Application of nonlinear dynamics theory to understanding normal and pathologic voices in humans, Phil. Trans. R. Soc. B 380 (1923) (2025) http://dx.doi.org/10.1098/rstb.2024.0018.

[12] M. Echternach, et al., Biomechanics of sound production in high-pitched classical singing, Sci. Rep. 14 (1) (2024) 13132, http://dx.doi.org/10.1038/s41598-024-62598-8.

[13] M. Köberlein, et al., Investigation of resonance strategies of high pitch singing sopranos using dynamic three-dimensional magnetic resonance imaging, J. Acoust. Soc. Am. 150 (6) (2021) 4191–4202, http://dx.doi.org/10.1121/10.0008903.

[14] M. Semmler, et al., Clinical relevance of endoscopic three-dimensional imaging for quantitative assessment of phonation, Laryngoscope 128 (10) (2018) 2367–2374, http://dx.doi.org/10.1002/lary.27165.

[15] J. Fischer, et al., Sub-millisecond 2D MRI of the vocal fold oscillation using single-point imaging with rapid encoding, Magn. Reson. Mater. Phys. Biology Med. 35 (2) (2022) 301–310, http://dx.doi.org/10.1007/s10334-021-00959-4.

[16] W. Jiang, X. Zheng, Q. Xue, Computational modeling of fluid-structure-acoustics interaction during voice production, Front. Bioeng. Biotechnol. 5 (FEB) (2017) http://dx.doi.org/10.3389/fbioe.2017.00007.

[17] J. Yang, et al., Fully-coupled aeroelastic simulation with fluid compressibility — For application to vocal fold vibration, Comput. Methods Appl. Mech. Engrg. 315 (2017) 584–606, http://dx.doi.org/10.1016/j.cma.2016.11.010.

[18] D. Bodaghi, et al., Effect of supraglottal acoustics on fluid-structure interaction during human voice production, J. Biomech. Eng. 143 (4) (2021) http://dx.doi.org/10.1115/1.4049497.

[19] S. Falk, et al., 3D-FV-FE aeroacoustic larynx model for investigation of functional based voice disorders, Front. Physiol. 12 (2021) 616985, http://dx.doi.org/10.3389/fphys.2021.616985.

[20] P. Hájek, et al., Finite-element modeling of vocal fold self-oscillations in interaction with vocal tract: Comparison of incompressible and compressible flow model, Appl. Comput. Mech. 15 (2) (2021) 133–152, http://dx.doi.org/10.24132/acm.2021.672.

[21] M. Dölinger, et al., Overview on state-of-the-art numerical modeling of the phonation process, Acta Acust. 7 (2023) 25, http://dx.doi.org/10.1051/aacus/2023014.

[22] M. Feistauer, et al., DGFEM for dynamical systems describing interaction of compressible fluid and structures, J. Comput. Appl. Math. 254 (2013) 17–30, http://dx.doi.org/10.1016/j.cam.2013.03.028.

[23] T.E. Shurtz, S.L. Thomson, Influence of numerical model decisions on the flow-induced vibration of a computational vocal fold model, Comput. Struct. 122 (2013) 44–54, http://dx.doi.org/10.1016/j.compstruc.2012.10.015.

[24] P. Svacek, J. Horáček, Finite element approximation of flow induced vibrations of human vocal folds model: Effects of inflow boundary conditions and the length of subglottal and supraglottal channel on phonation onset, Appl. Math. Comput. 319 (2018) 178–194, http://dx.doi.org/10.1016/j.amc.2017.02.026.

[25] H. Sadeghi, et al., Computational models of Laryngeal aerodynamics: Potentials and numerical costs, J. Voice 33 (4) (2019) 385–400, http://dx.doi.org/10.1016/j.jvoice.2018.01.001.

[26] R. Mittal, G. Iaccarino, Immersed boundary methods, Annu. Rev. Fluid Mech. 37 (2005) 239–261, http://dx.doi.org/10.1146/annurev.fluid.37.061903.175743.

[27] H. Luo, et al., An immersed-boundary method for flow-structure interaction in biological systems with application to phonation, J. Comput. Phys. 227 (22) (2008) 9303–9332, http://dx.doi.org/10.1016/j.jcp.2008.05.001.

[28] R. Verzicco, Immersed boundary methods: Historical perspective and future outlook, Annual Rev. Fluid Mech. 55 (2023) 129–155, http://dx.doi.org/10.1146/annurev-fluid-120720-022129.

[29] W. Jiang, et al., Computational modeling of voice production using excised canine larynx, J. Biomech. Eng. 144 (2) (2022) http://dx.doi.org/10.1115/1.4052226.

[30] M.J. Krause, et al., Particle flow simulations with homogenised lattice Boltzmann methods, Particuology 34 (2017-10) 1–13, http://dx.doi.org/10.1016/j.partic.2016.11.001.

[31] R. Trunk, et al., Towards the simulation of arbitrarily shaped 3D particles using a homogenised lattice Boltzmann method, Comput. & Fluids (2018) http://dx.doi.org/10.1016/j.compfluid.2018.02.027.

[32] A. Kummerländer, et al., Efficient wall-modelled large eddy simulation of rotors using homogenized lattice Boltzmann methods, Internat. J. Numer. Methods Heat Fluid Flow (2026) http://dx.doi.org/10.1108/HFF-09-2025-0724.

[33] P. Gomez, et al., Physical parameter estimation from porcine ex vivo vocal fold dynamics in an inverse problem framework, Biomech. Model. Mechanobiol. 17 (3) (2018) 777–792, http://dx.doi.org/10.1007/s10237-017-0992-5.

[34] M.J. Krause, et al., OpenLB—Open source lattice Boltzmann code, Comput. Math. Appl. (2021) http://dx.doi.org/10.1016/j.camwa.2020.04.033.

[35] A. Kummerländer, et al., OpenLB release 1.8: Open source lattice boltzmann code, 2025, http://dx.doi.org/10.5281/zenodo.15270117.

[36] A. Kummerländer, et al., Implicit propagation of directly addressed grids in lattice Boltzmann methods, Concurr. Comput.: Pr. Exp. (2023) http://dx.doi.org/10.1002/cpe.7509.

[37] S. Simonis, et al., Homogenized Lattice Boltzmann Methods for Fluid Flow Through Porous media – part I: Kinetic Model Derivation, ESAIM M2AN, 2025, http://dx.doi.org/10.1051/m2an/2025005.

[38] C. Coreixas, et al., Recursive regularization step for high-order lattice Boltzmann methods, Phys. Rev. E 96 (2017) http://dx.doi.org/10.1103/PhysRevE.96.033306.

[39] J. Jacob, O. Malaspinas, P. Sagaut, A new hybrid recursive regularised Bhatnagar–Gross–Krook collision model for Lattice Boltzmann method-based large eddy simulation, J. Turbul. 19 (11–12) (2018) http://dx.doi.org/10.1080/14685248.2018.1540879.

[40] S. Ito, et al., Geometry reconstruction from magnetic resonance velocimetry measurementsvia solving an inverse fluid flow problem, 2025, http://dx.doi.org/10.2139/ssrn.5313346.

[41] S. Simonis, Lattice Boltzmann Methods for Partial Differential Equations (Ph.D. thesis), Karlsruhe Institute of Technology (KIT), 2023, http://dx.doi.org/10.5445/IR/1000161726.

[42] A. Kummerländer, et al., Optimization of single node load balancing for lattice Boltzmann method on heterogeneous high performance computers, J. Parallel Distrib. Comput. 206 (2025) 105169, http://dx.doi.org/10.1016/j.jpdc.2025.105169.

[43] G. Chourdakis, et al., preCICE v2: A sustainable and user-friendly coupling library, Open Res. Eur. 2 (51) (2022) http://dx.doi.org/10.12688/openreseurope.14445.2.

[44] J. Donhauser, B. Tur, M. Döllinger, Neural network-based estimation of biomechanical vocal fold parameters, Front. Physiol. 15 (2024) 1282574, http://dx.doi.org/10.3389/fphys.2024.1282574.

[45] S. Thomson, L. Mongeau, S. Frankel, Physical and numerical flow-excited vocal fold models, in: Proceedings of the Third International Workshop on Models and Analysis of Vocal Emissions for Biomedical Applications, Florence, Italy, 2003, 10–12 December 2003.

[46] R.C. Scherer, et al., Intraglottal pressure profiles for a symmetric and oblique glottis with a divergence angle of 10 degrees, J. Acoust. Soc. Am. 109 (4) (2001) 1616–1630, http://dx.doi.org/10.1121/1.1333420, ISSN 0001-4966, 1520-8524.

[47] S.D. Gray, et al., Biomechanical and histologic observations of vocal fold fibrous proteins, Ann. Otol. Rhinol. Laryngol. 109 (1) (2000) 77–85, http://dx.doi.org/10.1177/000348940010900115, ISSN 0003-4894, 1943-572X.

[48] M. Döllinger, et al., Assessment of local vocal fold deformation characteristics in an *in vitro* static tensile test, J. Acoust. Soc. Am. 130 (2) (2011) 977–985, http://dx.doi.org/10.1121/1.3605671, ISSN 0001-4966, 1520-8524.

[49] J.E. Kelleher, et al., Optical measurements of vocal fold tensile properties: Implications for phonatory mechanics, J. Biomech. 44 (9) (2011) 1729–1734, http://dx.doi.org/10.1016/j.jbiomech.2011.03.037.

[50] K. Ishizaka, J.L. Flanagan, Synthesis of voiced sounds from a two-mass model of the vocal cords, Bell Syst. Tech. J. 51 (6) (1972) 1233–1268, http://dx.doi.org/10.1002/j.1538-7305.1972.tb02651.x.

[51] L.P. Fulcher, et al., Negative Coulomb damping, limit cycles, and self-oscillation of the vocal folds, Am. J. Phys. 74 (5) (2006) 386–393, http://dx.doi.org/10.1119/1.2173272, ISSN 0002-9505, 1943-2909.

[52] W. Schroeder, K. Martin, B. Lorensen, The Visualization Toolkit (4th ed.), Kitware, 2006.

[53] U. Ayachit, The ParaView Guide: Updated for Paraview Version 4.3, Full color version, Kitware Inc, Clifton Park, NY, 2015,

[54] C.D. Hansen, C.R. Johnson, The Visualization Handbook, Elsevier-Butterworth Heinemann, Amsterdam Boston, 2005.

[55] A.M. Kist, et al., A Deep Learning Enhanced Novel Software Tool for Laryngeal Dynamics Analysis, J. Speech Lang. Hear Res. 64 (6) (2021) 1889–1903, http://dx.doi.org/10.1044/2021_JSLHR-20-00498, ISSN 1092-4388, 1558-9102URL: http://pubs.asha.org/doi/10.1044/2021_JSLHR-20-00498.

[56] R. Patel, D. Dubrovskiy, M. Döllinger, Characterizing vibratory kinematics in children and adults with high-speed digital imaging, J. Speech Lang. Hear Res. 57 (2) (2014) http://dx.doi.org/10.1044/2014_JSLHR-S-12-0278, ISSN 1092-4388, 1558-9102.

[57] R.J. Baken, R.F. Orlikoff, Clinical Measurement of Speech and Voice, second [Nachdr.], Delmar Cengage Learning, Clifton Park, NJ, 2010.

[58] E.B. Holmberg, R.E. Hillman, J.S. Perkell, Glottal airflow and transglottal air pressure measurements for male and female speakers in soft, normal, and loud voice, J. Acoust. Soc. Am. 84 (2) (1988) 511–529, http://dx.doi.org/10.1121/1.396829, ISSN 0001-4966, 1520-8524.

[59] S.-G. Wang, et al., A new videokymography system for evaluation of the vibration pattern of entire vocal folds, Auris. Nasus. Larynx. 43 (3) (2016) 315–321, http://dx.doi.org/10.1016/j.anl.2015.10.002, URL: https://linkinghub.elsevier.com/retrieve/pii/S0385814615002278.

[60] Q. Qiu, et al., An automatic method to quantify the vibration properties of human vocal folds via videokymography, Folia Phoniatr. et Logop. 55 (3) (2003) 128–136, http://dx.doi.org/10.1159/000070724, ISSN 1021-7762, 1421-9972.

[61] M. Lasota, et al., Impact of the sub-grid scale turbulence model in aeroacoustic simulation of human voice, Appl. Sci. 11 (4) (2021) 1970, http://dx.doi.org/10.3390/app11041970.

[62] E. Sundström, et al., Fluid-structure interaction analysis of aerodynamic and elasticity forces during vocal fold vibration, J. Voice 39 (2) (2025) 293–303, http://dx.doi.org/10.1016/j.jvoice.2022.08.030.

[63] L. Bailly, et al., Influence of a constriction in the near field of the vocal folds: physical modeling and experimental validation, J. Acoust. Soc. Am. 124 (5) (2008) 3296–3308, http://dx.doi.org/10.1121/1.2977740.

[64] H. Sadeghi, et al., Aerodynamic impact of the ventricular folds in computational larynx models, J. Acoust. Soc. Am. 145 (4) (2019) 2376–2387, http://dx.doi.org/10.1121/1.5098775.

[65] T. Yoshinaga, Z. Zhang, Effects of false vocal fold adduction and aryepiglottic sphincter narrowing on the voice source in a three-dimensional voice production model, J. Acoust. Soc. Am. 157 (4) (2025) 2408–2421, http://dx.doi.org/10.1121/10.0036359.

[66] L. Gühring, et al., Influence of flow rate and fiber tension on dynamical, mechanical and acoustical parameters in a synthetic larynx model with integrated fibers, Front. Physiol. 15 (2024) 1455360, http://dx.doi.org/10.3389/fphys.2024.1455360.

[67] B. Tur, et al., Effect of ligament fibers on dynamics of synthetic, self-oscillating vocal folds in a biomimetic Larynx Model, Bioengineering 10 (10) (2023) 1130, http://dx.doi.org/10.3390/bioengineering10101130.

[68] H.E. Gunter, et al., Measurement of vocal fold collision forces during phonation: Methods and preliminary data, J. Speech Lang. Hear. Res. 48 (3) (2005) 567–576, http://dx.doi.org/10.1044/1092-4388(2005/039), ISSN 1092-4388, 1558-9102URL: http://pubs.asha.org/doi/10.1044/1092-4388%282005/039%29.

[69] A. Lagier, et al., Larynx under ultra-high subglottal pressure: measure of contact force between vocal folds in excised human larynges, in: 11th Pan-European Voice Conference (PEVOC), Florence, Italy, 2015.

[70] J. Michaud-Dorko, et al., Volumetric supraglottal jet fow feld analysis in synthetic multilayered self-oscillating vocal fold model, Exp. Fluids 66 (2025) 7.1–7.18, http://dx.doi.org/10.1007/s00348-024-03936-4.